Anisotropic electronic transport and Rashba effect of the two-dimensional electron system in (110) $SrTiO_3$-based heterostructures

K. Wolff, R. Eder, R. Schäfer, R. Schneider, and D. Fuchs
Karlsruher Institut für Technologie, Institut für Festkörperphysik, 76021 Karlsruhe, Germany

(Received 8 March 2018; revised manuscript received 31 July 2018; published 11 September 2018)

The two-dimensional electron system in (110) $Al_2O_{3-\delta}/SrTiO_3$ heterostructures displays anisotropic electronic transport. Largest and lowest conductivity and electron mobility μ are observed along the [001] and [1$\bar{1}$0] directions, respectively. The anisotropy of the sheet resistance and μ likewise leads to a distinct anisotropic normal magnetotransport (MR) for $T < 30$ K. However, at temperatures $T < 5$ K and magnetic field $B < 2$ T MR is dominated by weak antilocalization. Despite the rather strong anisotropy of the Fermi surfaces, the in-plane anisotropic magnetoresistance (AMR) displays twofold noncrystalline anisotropy. However, the AMR amplitude is found to be anisotropic with respect to the current direction, leading to a 60% larger AMR amplitude for current I along the [001] direction compared to I parallel to [1$\bar{1}$0]. Tight-binding calculations evidence an anisotropic Rashba-induced band splitting with dominant linear k dependence. In combination with semiclassical Boltzmann theory, the noncrystalline AMR is well described, despite the anisotropic Fermi surface.

DOI: 10.1103/PhysRevB.98.125122

I. INTRODUCTION

The two-dimensional electron system (2DES) formed at the interface of the band insulators $LaAlO_3$ (LAO) and $SrTiO_3$ (STO) displays many intriguing features such as superconductivity, spin-orbit interaction (SOI), and multiple quantum criticality [1–3], and has thus made LAO/STO a prototypical system for studying low-dimensional strongly correlated electron systems. Magnetic properties are reported alike [4], however, believed to arise rather from extrinsic sources like oxygen vacancies and strain.

In (001)-oriented LAO/STO, the sheet carrier concentration n_s can be tuned by electric field gating through a Lifshitz transition [5] occurring at a critical sheet carrier concentration $n_c \approx 1.7 \times 10^{13}$ cm^{-2}, where itinerant electrons change from populating only Ti derived 3d t_{2g} orbitals with d_{xy} symmetry to occupying also the d_{xz}, d_{yz} orbitals. These bands result in a highly elliptical Fermi surface oriented along crystalline directions and may give reason for the observation of crystalline anisotropic electronic properties. In addition, localized magnetic moments, pinned to specific d_{xy} orbitals, may lead to crystalline anisotropy as well and may complicate anisotropic electronic transport. The coexistence of localized charge carriers close to the interface and itinerant d electrons may lead to fascinating phenomena such as nonisotropic magnetotransport or magnetic exchange. However, it is not clear whether interaction between these localized magnetic moments and mobile charge carriers really happens.

The SOI in (001) LAO/STO results in a noncrystalline twofold anisotropic in-plane magnetoresistance (AMR) [6]. Interestingly, for $n_s > n_c$ sometimes a more complex AMR with a fourfold crystalline anisotropy is reported, which is discussed in terms of a tunable coupling between itinerant electrons and electrons localized in d_{xy} orbitals at Ti vacancies [7]. However, the appearance of a crystalline AMR with increasing n_s is not always evident and raises the question about its microscopic origin. More recently, a giant crystalline AMR of up to 100% was reported in (110)-oriented LAO/STO [8]. Here AMR was attributed to orbital polarization caused by oxygen vacancies. With respect to both, namely, fundamental aspects such as the possible simultaneous appearance of magnetism and superconductivity and applications in the field of spintronics, a more fundamental knowledge about the origin of anisotropic magnetotransport is highly desired. Measurements of the AMR in a rotating in-plane magnetic field are well suited to probe crystalline anisotropy and symmetry of a 2DES and are a promising tool to elucidate magnetic properties because of their high sensitivity toward spin-texture and SOI [9].

To investigate the microscopic origin of the anisotropic electronic properties of the 2DES of STO-based heterostructures, we studied in detail the electronic transport of the 2DES formed at the interface of spinel-type $Al_2O_{3-\delta}$ and (110)-oriented STO (AO/STO). The presence of oxygen vacancies [10] promoting localized d_{xy} electrons in combination with the anisotropic band structure of (110) STO surface [11] makes (110) AO/STO very suitable for these experiments. The heterostructures were produced by standard pulsed laser deposition, and characterization of the electronic transport was done by sheet resistance measurements. Band structure calculations were carried out using linear combination of atomic orbitals (LCAO) approximation to model band structure and Fermi surface properties of (110) AO/STO. AMR was deduced using semiclassical Boltzmann theory. Surprisingly, despite the anisotropy of the electronic band structure and SOI, compared to (001) LAO/STO, we did not observe indications for a crystalline AMR in (110) AO/STO. The AMR displays twofold noncrystalline anisotropic behavior. Contributions to the electronic transport from the different Fermi surface sheets as well as the anisotropy of the Fermi surfaces itself are sensitively affected by n_s. However, a variation of n_s

($0.02 \leqslant n_s \leqslant 0.06$) does not lead to a crystalline behavior of the AMR.

II. EXPERIMENTAL

Sample preparation has been carried out by depositing $Al_2O_{3-\delta}$ films onto (110)-oriented STO substrates with a thickness of about 15 nm at a substrate temperature of $T_s = 250^\circ$ C by pulsed laser deposition [12]. To achieve an atomically flat, single-type terminated substrate surface, the substrates are annealed at $T = 950^\circ$ C for 5 h in flowing oxygen. The (110) STO surface can be terminated by a SrTiO or an oxygen layer, see Fig. 1(a), where the cation composition at the interface should be always the same in case of single-type termination. Annealing results in a stepped surface topography with a step height of about 2.7 Å and a step width of 80 nm, see Fig. 1(b). Oxygen partial pressure during $Al_2O_{3-\delta}$ deposition and cool-down process was $p(O_2) = 10^{-6}$ mbar. Prior to the deposition, microbridges with a length of 100 μm and a width of 20 μm in Hall bar geometry have been patterned along specific crystallographic directions using a CeO_2 hard mask technique [13], see Fig. 1(c). The microbridges are labeled from A to E, with angle $\varphi = 0^\circ$, 22.5°, 45°, 67.5°, and 90° toward the [1$\bar{1}$0] direction, i.e., A and E parallel to [1$\bar{1}$0] and [001] directions, respectively.

The sheet resistance R_s was measured using a physical property measurement system (PPMS) from Quantum Design in the temperature and magnetic field ranges 2 K $\leqslant T \leqslant$ 300 K and $0 \leqslant B \leqslant 14$ T. To avoid charge carrier activation by light [14,15], alternating current measurements ($I_{ac} = 3\mu$A) were started not before 12 h after loading the samples to the PPMS. The magnetoresistance, MR $= [R_s(B) - R_s(0)]/R_s(0)$, and AMR $= [R_s(B_{ip}, \phi) - R_s(B_{ip}, 0)]/R_s(B_{ip}, 0)$, have been measured with magnetic field normal (B) and parallel (B_{ip}) to the interface, respectively. For measuring AMR with rotating in-plane magnetic field $B_{ip}(\phi)$, a sample rotator was used. The angle ϕ between B_{ip} and [001]-direction was varied from 0°–360°. Special care has been taken to minimize sample wobbling in the apparatus. Residual tilts (1°–2°) of the surface, normal with respect to the rotation axis, which produces a perpendicular field component oscillating in sync with ϕ could be identified by comparison of $R_s(B_{ip}, \phi)$ for different microbridges and could therefore be corrected properly.

III. RESULTS AND DISCUSSION

A. Temperature dependence of the anisotropic electronic transport

The anisotropic electronic band structure of the 2DES found in (110)-oriented LAO/STO heterostructures [8] and at the reconstructed surface of (110)-oriented STO [11] obviously lead to anisotropic electronic transport [16,17]. The lowest electronic subbands along the [1$\bar{1}$0] direction (along $\Gamma - M$) display much weaker dispersion and smaller bandwidth compared to the [001] direction (along $\Gamma - Z$), which typically results in larger resistance for current I direction along the [1$\bar{1}$0] direction [8,17]. The electronic transport in (110) AO/STO displays distinct anisotropy as well. The T dependence of the sheet resistance R_s along different crystallographic directions is shown in Fig. 2(a). For all the

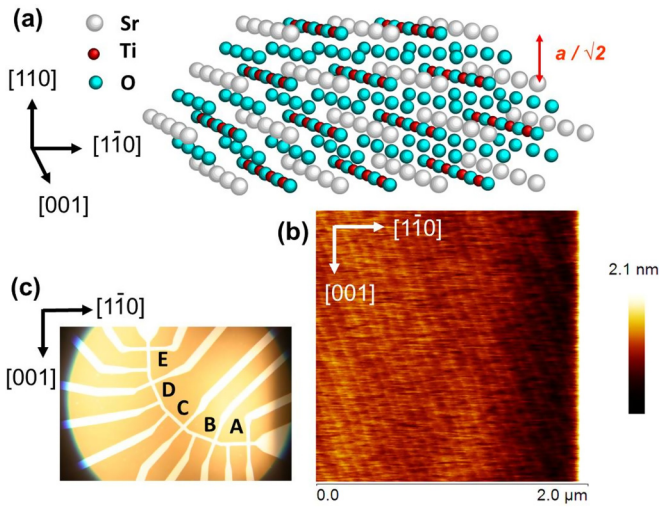

FIG. 1. (a) Schematic of the crystal structure of STO. In case of (110) orientation, the surface can be terminated with a SrTiO or oxygen layer. The spacing of the cation layers is $a/\sqrt{2}$, where $a = 3.905$ Å is the cubic lattice parameter of STO. Crystallographic directions and atom labels are indicated. (b) Surface topography before $Al_2O_{3-\delta}$ deposition characterized by atomic force microscopy. The image was taken on microbridge A. (c) Optical micrograph of a patterned sample. Sharp contrast between AO/CeO_2 (dark) and AO/STO (bright) enables identifying microbridges labeled alphabetically from A–E.

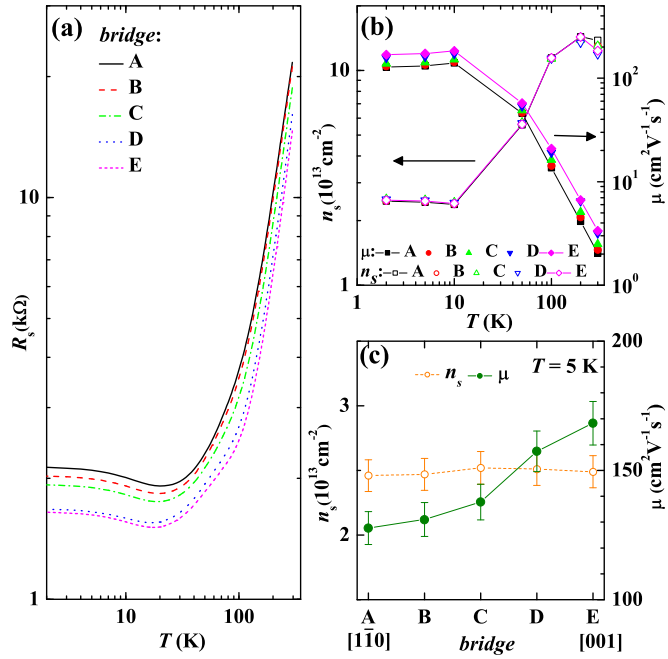

FIG. 2. (a) Sheet resistance R_s versus T for microbridges A – E (from top to bottom) with an angle $\varphi = 0^\circ$, 22.5°, 45°, 67.5°, and 90° toward the [1$\bar{1}$0] direction, i.e., $A \parallel$ [1$\bar{1}$0] and $E \parallel$ [001]. (b) Sheet carrier density n_s, left scale, and Hall mobility μ, right scale, versus T for A–E. (c) n_s, left scale, and μ, right scale for bridge A–E at $T = 5$ K.

microbridges, R_s decreases with deceasing T nearly $\propto T^2$ down to about 100 K and shows a shallow minimum around 20 K. The T dependence is very similar to that observed in (001) AO/STO and is likely explained by strong renormalization due to electron-phonon interaction and impurity scattering [18,19]. The resistivity ratio between 300 K and 10 K amounts to about 20, which is nearly the same as that of (001) AO/STO. R_s steadily decreases from A ($I \parallel [1\bar{1}0]$) to E ($I \parallel [001]$) with increasing φ at constant T throughout the complete T range. Obviously, anisotropic transport is not only restricted to low temperatures $T < 10$ K, where usually impurity scattering dominates R_s. Moreover, the anisotropy between A and E, $[R_s(A) - R_s(E)]/R_s(E)$ is largest at $T =$ 300 K amounting to 47% and decreases with decreasing T to 29% at $T = 5$ K. This rather small T dependence indicates that the intrinsic anisotropic electronic band structure is very likely the dominant source for the anisotropic transport. In contrast, anisotropic transport in (001) AO/STO is extrinsic in nature and is found only at low T, where it is caused mainly by anisotropic impurity scattering due to an inhomogeneous distribution of ⟨110⟩ lattice dislocations [20]. However, the amount and anisotropy of the distribution of such defects likely depends on crystal orientation and may change from crystal to crystal. Since the dislocation lines are preferentially aligned along (110) lattice planes, impurity scattering would be rather enhanced along the [001] than the $[1\bar{1}0]$ direction, leading to an anisotropic transport opposite to that displayed in Fig. 2(a). Hence, we assume that the anisotropic behavior of R_s is mainly caused by an intrinsic electronic anisotropy.

To extract sheet carrier density n_s and mobility μ, Hall measurements have been carried out in a magnetic field $-14\ \text{T} \leqslant B \leqslant 14\ \text{T}$ applied normal to the interface for $2\ \text{K} \leqslant T \leqslant 300\ \text{K}$. For $T < 30$ K, the Hall resistance R_{xy} becomes slightly nonlinear, indicating multitype carrier transport. However, n_s, which we determined from the asymptotic value of R_{xy} at high fields, i.e., the total n_s, usually deviates by less than 10% from n_s extracted from R_{xy} in the limit of $B = 0$. A nonlinear Hall resistance at low T is often reported for STO-based heterostructures and discussed in terms of the large and nonlinear dielectric response of STO and carrier depth distribution [21]. (001)-oriented AO/STO heterostructures prepared under similar conditions display Berezinskii-Kosterlitz-Thouless transition and weak antilocalization (WAL) [12], which strongly hints to a two-dimensional confinement of the electron liquid. For the (110) AO/STO samples, WAL (see Sec. II B) is of the same magnitude, indicating confined two-dimensional behavior of the charge carriers as well. For that reason, we are confident that electronic transport is not dominated by bulk carriers. However, we cannot give any information of the thickness of the metallic interfacial layer. It may differ from LAO/STO material and, because of the different electron subband structure, possibly also from (001)-oriented samples.

In Fig. 2(b), the total n_s and the Hall mobility, calculated by $\mu = (R_s(B = 0) \times n_s \times e)^{-1}$, where e is the elementary charge, are shown as functions of T. n_s decreases with decreasing T from about 1.3×10^{14} cm^{-2} at $T = 300$ K to 2.5×10^{13} cm^{-2} at $T = 5$ K and is well comparable to that of (110) LAO/STO [10].

In contrast to the T dependence of n_s, μ increases from about 2.5 cm^2/(Vs) with decreasing T to 150 cm^2/(Vs). The T dependence of n_s and μ is well comparable to that observed in 2DES of (001) STO-based heterostructures [20,22,23]. As expected from R_s, the maximum anisotropy of n_s and μ is observed at $T = 300$ K, amounting to 16% and 65%, respectively, and decreases to 2% and 34% at $T = 5$ K. Therefore, the anisotropy of R_s at low T is mainly caused by the anisotropy of μ, whereas n_s for the different microbridges A–E are roughly the same. The superior role of μ with respect to electronic anisotropy is demonstrated in Fig. 2(c) where n_s and μ are plotted for A–E at $T = 5$ K. n_s differs only a little for the different microbridges. In contrast, μ steadily increases from A to E with increasing φ and shows the highest mobility for bridge E, i.e., along the [001] direction. The results are reasonable with respect to the anisotropic band structure and Fermi surface of (110) AO/STO, which will be discussed in more detail in Sec. III C.

B. Magnetotransport

Measurements of the MR and AMR with magnetic field direction normal or parallel to the interface, respectively, are often used to characterize SOI in low-dimensional electron systems. In STO-based 2DES, the Rashba-type SOI usually leads to a WAL of the charge carrier transport at low T [2], resulting in a logarithmic T dependence of R_s [24]. However, the quantum coherence can be destroyed by applying moderate magnetic fields leading to a distinct positive MR [25].

For $T \geqslant 50$ K, the MR of (110) AO/STO is rather small, less than 2%, and displays no distinct anisotropy with respect to the crystallographic direction. For $T < 50$ K, MR starts to increase with respect to amplitude and anisotropy. In Fig. 3, MR is shown for the microbridges A–E, for $T = 10$ K and 2 K. For $T = 10$ K, MR is positive and amounts to about 10%. The B dependence of MR indicates orbital motion of free carriers due to the Lorentz force, i.e., classical Lorentz scattering (LS) as the dominant scattering mechanism, where MR is well described by the Kohler form: $\text{MR} \propto (1/R_0) \times (\frac{B}{w})^2/(1 + (\frac{B}{w})^2)$, with the zero-field resistance R_0 [26]. Fits to the Kohler form are shown by solid lines in Fig. 3(a). MR displays clear anisotropic behavior with respect to the microbridges, showing a systematic increase from A to E. This is very likely related to the decrease of the zero-field resistance from A to E, see Fig. 2(a).

For $T = 2$ K, an additional contribution to the positive MR appears. However, significant changes to MR are restricted to the low field region, $B < 8$ T. As mentioned above, in 2DES, charge transport in the diffusive regime is well described by the 2D WAL theory [24]. The quantum corrections to the conductivity arise from the interference of electron waves scattered along closed paths in opposite directions. Phase coherence is destroyed if the applied magnetic field, which results in a phase shift between the corresponding amplitudes, exceeds a critical value. An estimation for the field limit $B^* = \hbar/(2el_m^2)$ can be deduced from the electron mean free path $l_m = \frac{\hbar}{e}\sqrt{2\pi n_s}\mu$ of the sample. For our sample, we obtain $l_m = 12$ nm, which results in a field limit of about 2 T.

Zeeman corrections to the WAL are taken into account by the Maekawa and Fukuyama (MF) theory [25], which

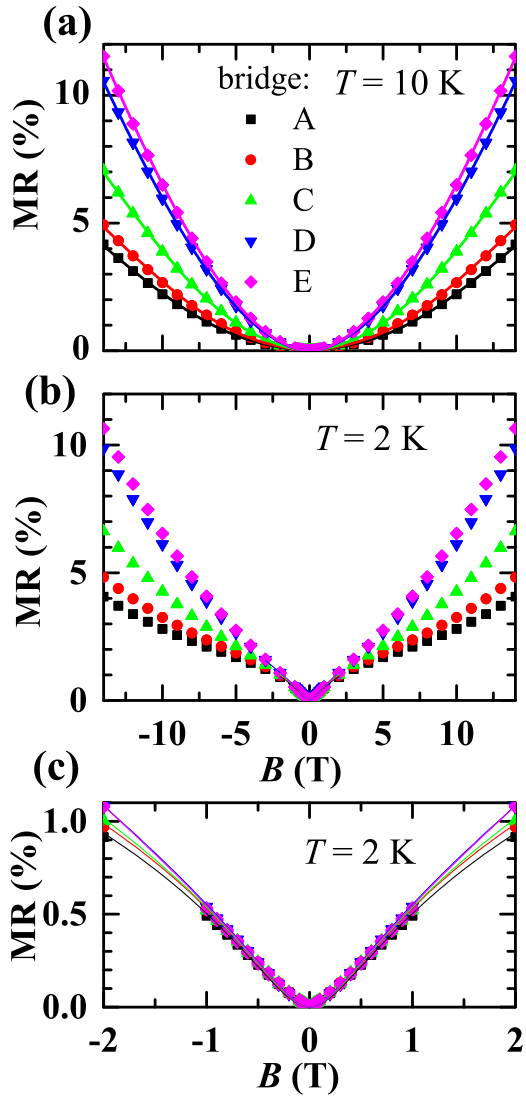

FIG. 3. Magnetoresistance MR for the different microbridges A–E at $T = 10$ K (a) and 2 K (b) versus magnetic field B applied perpendicular to the interface. (c) MR at $T = 2$ K in the low-field range for $B < B^*$. Fits to the data with respect to the Kohler form and MF expression are shown by solid lines, see text.

is usually used to describe the B dependence of the MR in LAO/STO and AO/STO [2,20]. The parameters of the MF expression are the inelastic field B_i, the spin-orbit field B_{so}, and the electron g factor, which enters into the Zeeman corrections.

For $B \leqslant 2$ T, MR at 2 K is well described by LS and WAL. Fits to the data, using the MF-based expression given in Ref. [2] in combination with a Kohler term, are shown in Figs. 3(b) and 3(c) by solid lines.

The WAL fitting results in parameters $B_i \approx 180$ mT and $B_{so} \approx 0.6$ T. Within the experimental resolution and the limited field range, WAL effect appears to be nearly the same for all the microbridges. Zeeman corrections to MR have been found to play only a minor role for the applied magnetic fields. The magnitude of B_i and B_{so} are well comparable to those found in (001) AO/STO and LAO/STO, where Rashba-type SOI has been identified as the dominant source of spin-orbit coupling.

In comparison to WAL, contributions from LS to MR at 2 K are rather small for $B < 2$ T. However, for $B > 8$ T, where WAL can usually be neglected, LS dominates MR again. Interestingly, in comparison to the anisotropy of MR with respect to the microbridges for $B > 8$ T and at $T = 10$ K, the anisotropy of MR at 2 K is slightly decreased. In contrast, the anisotropy of R_0, μ, and n_s with respect to the current direction are well comparable for $T = 10$ K and 2 K, or even slightly larger at 2 K and likely do not explain that behavior. It might be suggested that Rashba-type SOI not only influences MR by WAL at low magnetic fields but also at higher fields, where WAL should be absent.

Anisotropic Rashba splitting was indeed observed by angle-resolved photoemission (ARPES) experiments on (110) STO surfaces [11] and discussed for (110) LAO/STO heterostructures [8,16]. The influence of SOI and Rashba effect on magnetotransport can be studied more specifically, if the magnetic field is applied parallel to the interface where changes of the MR by WAL are negligible.

Applying the magnetic field parallel to the interface at an angle ϕ with respect to the [001] direction, $B_{ip}(\phi)$, results in a strong field-induced directional anisotropy of the resistance $R_s(B, \phi)$, i.e., an AMR. Figures 4(a) and 4(b) document $R_s(B_{ip}, \phi)$ versus ϕ for different B_{ip} at $T = 2$ K for bridge A and E, respectively. $R_s(B_{ip}, \phi)$ shows a two-fold anisotropic behavior. The absolute value of R_s first increases up to $B_{ip} \approx 5$ T, where the positive magnetoresistance is largest, and then decreases turning to a negative magnetoresistance for $B_{ip} \geqslant 10$ T. The amplitudes of the oscillations steadily increase with increasing B_{ip}. For $B_{ip} < 1$ T, the amplitude is rather small and displays a crystalline anisotropy, i.e., maxima of $R_s(B_{ip}, \phi)$ always appear at $\phi = 90°$ for B_{ip} perpendicular to the [001] direction. In contrast, for $B_{ip} = 1$ T, the AMR behavior displays distinct noncrystalline anisotropy, i.e., maxima always occur for B_{ip} parallel to the current direction.

Noncrystalline anisotropic behavior was also found in (001) LAO/STO and AO/STO. In the framework of the Drude-Boltzmann theory, it was shown that a Rashba-type SOI in (001) LAO/STO induces a twofold noncrystalline anisotropy in the magnetoconductance [6], i.e., $\Delta\sigma = [\sigma(B_{ip}, \Theta) - \sigma(B_{ip}, 0)] \propto \sin^2(\Theta)$, where the amplitude of the oscillations should scale for moderate field strength with the square of the spin-orbit energy, i.e., $\Delta\sigma(\Theta = 90°)/\sigma_0 \propto \Delta_{so}^2$, where $\sigma_0 = \sigma(B_{ip}, 0)$ and Θ the angle between I and B_{ip}. Therefore, it is very likely, that the observed anisotropy of $R_s(B_{ip}, \phi)$ is caused by Rashba-type SOI alike.

The amplitude of the oscillations of $R_s(B_{ip}, \phi)$ increases with increasing magnetic field reaching an AMR of about 1% for A, i.e., along the $[1\bar{1}0]$ direction and 1.4% for E, parallel to the [001] direction for $B_{ip} = 14$ T. The different amplitudes likely indicate an anisotropic Rashba-type SOI. Note that the AMR is about one order of magnitude smaller as compared to the MR. In Figs. 4(c) and 4(d), the in-plane magnetoresistance $MR_{ip} = [R_s(B_{ip}, \Theta) - R_s(0, \Theta)]/R_s(0, \Theta)$ is plotted for A and E versus B_{ip} for field direction parallel ($\Theta = 0°$) and perpendicular ($\Theta = 90°$) to the current I direction, demonstrating the positive and negative magnetoresistance in more detail.

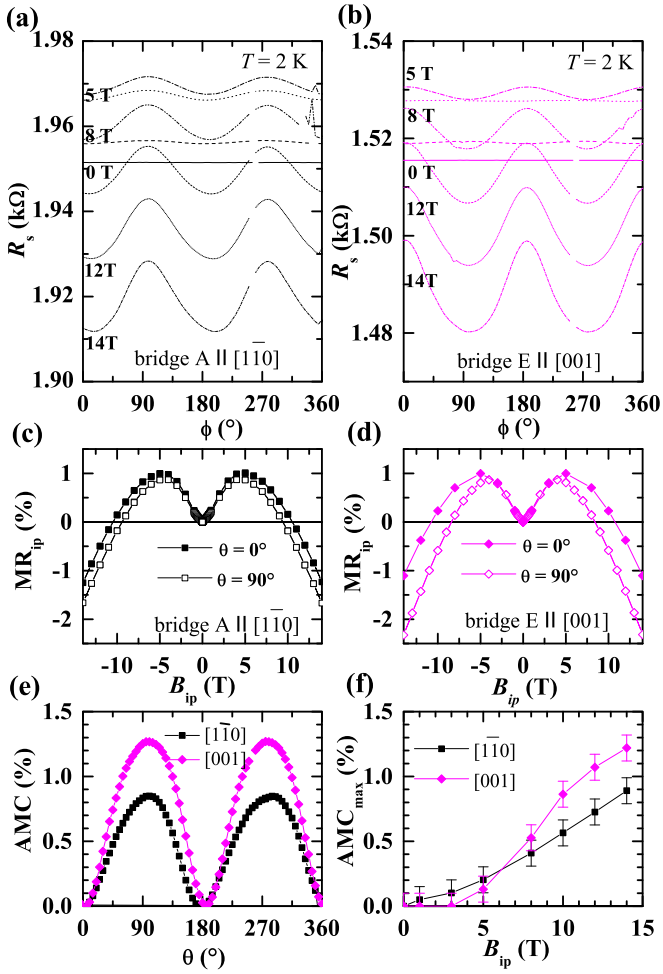

FIG. 4. AMR of (110) AO/STO at 2 K. R_s versus in-plane angle ϕ for different strengths of B_{ip} (0, 1, 3, 5, 8, 10, 12, and 14 T) for (a) bridge A, i.e., I parallel to the [1$\bar{1}$0] direction, and (b) bridge E, I being parallel to the [001] direction. The field strength $B_{\rm ip}$ is indicated exemplarily. In-plane magnetoresistance $MR_{\rm ip}$ versus $B_{\rm ip}$ for field direction parallel ($\Theta = 0^\circ$) and perpendicular ($\Theta = 90^\circ$) to current flow direction for (c) bridge A and (d) bridge E. (e) Anisotropic magnetoconductance AMC versus Θ, the angle between current I and $B_{\rm ip}$ for the [1$\bar{1}$0] and [001] directions for $B = 14$ T and $T = 2$ K. (f) The amplitude of the magnetoconductance oscillations $AMC_{\rm max}$ versus $B_{\rm ip}$ for the [1$\bar{1}$0] and the [001] directions. The minima of the magnetoconductance oscillations were found always at $\Theta = 0^\circ, 180^\circ$, i.e., $B_{\rm ip}$ parallel to the current direction.

The $MR_{\rm ip}$ for $\Theta = 0^\circ$ is only slightly larger compared to $\Theta = 90^\circ$. With increasing $B_{\rm ip}$, the $MR_{\rm ip}$ first increases, displaying a maximum positive magnetoresistance around 5 T. Then, the $MR_{\rm ip}$ decreases and even becomes negative for $B_{\rm ip}$ above about 10 T. The negative $MR_{\rm ip}$ at large fields possibly results from spin-polarized bands due to Zeeman effect, leading to a suppression of interband scattering with increasing B [27].

Figure 4(e) shows the anisotropic magnetoconductance $AMC = [\sigma(B_{\rm ip}, \Theta) - \sigma(B_{\rm ip}, 0)]/\sigma(B_{\rm ip}, 0)$ versus Θ for $I \parallel [1\bar{1}0]$ and $I \parallel [001]$ at $B_{\rm ip} = 14$ T and $T = 2$K. The maxima of the magnetoconductance oscillations $AMC_{\rm max}$ always appear at $\Theta = 90^\circ$ and 270°, i.e., $B_{\rm ip}$ perpendicular to the current direction. For the [001] direction, $AMC_{\rm max}$ amounts to about 1.3% and is distinctly larger compared to that of the [1$\bar{1}$0] direction ($\approx$0.8%). The field dependence of the amplitude $AMC_{\rm max}$ for the two orthogonal directions is shown in Fig. 4(f). Measurable magnetoconductance appears for $B_{\rm ip} > 3$ T and increases with field to 1.2% and 0.9% at 14 T for the [001] and [1$\bar{1}$0] directions, respectively. Rashba effect seems to increase with increasing $B_{\rm ip}$ and to be anisotropic with respect to crystallographic direction.

C. Theoretical modeling of the electronic band structure and magnetotransport

To obtain a better understanding of the measured electronic transport, especially the AMR behavior, we carried out tight-binding calculations to model the electronic subbandstructure of (110) AO/STO. Details of the linear combination of atomic orbitals (LCAO) calculations are given in the Appendix. The calculation yields the energy bands $E_{\nu,\mathbf{k}}$ where ν is the band index and $\mathbf{k}$ the wave vector in the rectangular Brillouin zone.

Figure 5 shows the band structure obtained in this way. The topmost panel shows the band structure in the absence of spin-orbit coupling and symmetry-breaking electric field, which roughly agrees with the band structure obtained by Wang *et al.* from a fit to their ARPES data [11] (the reason for the deviation is our modification of the nearest-neighbor hopping t for bonds in [001]direction, see the discussion in the Appendix). Since there is no mixing between the three t_{2g} orbitals, the bands can be classified according to the type of d orbital from which they are composed, whereby the bands derived from the d_{xz} and d_{yz} orbitals are degenerate. The dashed horizontal line gives the Fermi energy for an electron density of 0.40/unit cell or 1.8×10^{14} cm^{-2}. This is considerably higher than the electron densities studied here but corresponds roughly to the experiments by Wang *et al.* [11]. In the figure, one can identify the various subbands generated by the confinement of the electrons perpendicular to the interface. This hierarchy of subbands in fact extends to considerably higher energies than shown in the figure.

The two lower panels show the band structure for finite spin-orbit coupling and symmetry breaking electric field, but $B = 0$. One can recognize the two different manifestations of the Rashba effect discussed already by Zhong *et al.* [28]: the splitting of bands near Γ, which can be either $\propto|\mathbf{k}|$ or $\propto|\mathbf{k}|^3$ (see below), and the opening of gaps. The formation of gaps is particularly obvious at Γ, where the lowest d_{xy}-derived band along $\Gamma - \bar{M}$ combines with one of the d_{xz}/d_{yz}-derived bands along $\Gamma - \bar{Z}$ to form a mixed band whose minimum is shifted upward by $\approx$20 meV. The dashed horizontal line in the lower two panels gives E_F for an electron density of $n_e = 0.05$/unit cell or 2.3×10^{13} cm^{-2}, which is roughly appropriate for our experiment. We have verified that varying the density in the range $0.04/\text{unit cell} \leqslant n_e \leqslant 0.07/\text{unit cell}$ does not have a significant influence on the magnetoresistance discussed below. From now on, the labeling of bands is according to their energy, i.e., the lowest band is labeled 1 and so on. Figure 6 shows the differences $\Delta_{\nu,\nu'}(\mathbf{k}) = E_{\nu,\mathbf{k}} - E_{\nu',\mathbf{k}}$ and demonstrates the power-law behavior of the Rashba-induced band splitting for small $|\mathbf{k}|$. Thereby, the splitting along [1$\bar{1}$0] is linear, i.e., $\Delta_{\nu,\nu'}(\mathbf{k}) = C_{\nu,\nu'}\frac{ka}{\pi}$ with $C_{2,1} = 60.8$ meV and

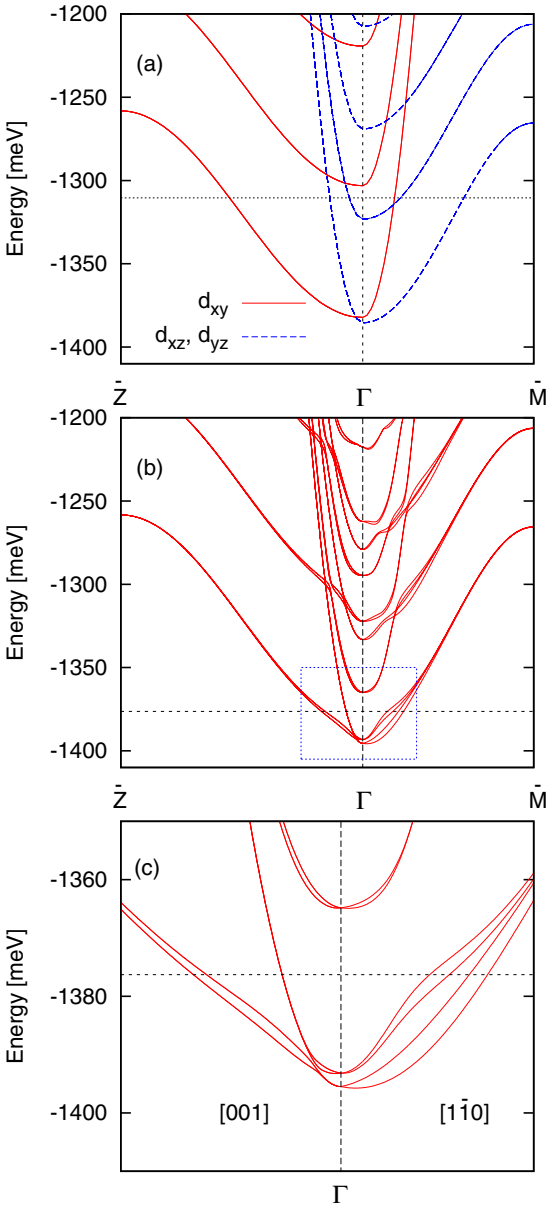

FIG. 5. LCAO band structure for the (110) AO/STO interface. (a) Band structure without spin-orbit coupling and symmetry-breaking electric field. All bands have twofold spin degeneracy, the horizonzal line is the Fermi energy for $n_e = 0.4$/unit cell. (b) Band structure including spin-orbit coupling and symmetry-breaking electric field, but $B = 0$. (c) Closeup of the box indicated in (b). In (b) and (c), the horizontal dashed line is the Fermi energy for $n_e = 0.05$/unit cell.

$C_{4,3} = 23.4$ meV, whereas along [001], the splitting between bands 3 and 4 still has this form with $C_{4,3} = 42.4$ meV, whereas the splitting between bands 1 and 2 now is cubic, $\Delta_{2,1}(k) = 2720\ \text{meV}(\frac{ka}{\pi})^3$. This highlights the anisotropy of the Rashba effect at the (110) AO/STO interface.

Figure 7 compares the Fermi surfaces for $n_e = 0.05$/unit cell in zero magnetic field and a field of 14 Tesla. All panels show the square $[-\frac{\pi}{4} : \frac{\pi}{4}] \otimes [-\frac{\pi}{4} : \frac{\pi}{4}]$, the field direction is along [001] (along [1$\bar{1}$0]) in the top four (bottom four) panels. In the absence of SOC and electric field, the Fermi surface

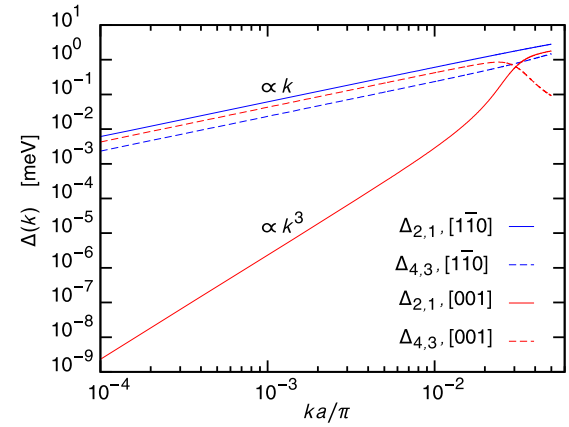

FIG. 6. Rashba-induced band splittings $\Delta_{\nu,\nu'}(\mathbf{k})$ near Γ along the two symmetry lines of the Brillouin zone.

would consist of two elliptical sheets centered at Γ, each of them twofold (spin-)degenerate. The ellipse derived from the d_{xz}/d_{yz} orbitals is elongated along the [1$\bar{1}$0] (or $\Gamma - \bar{M}$) direction, whereas the ellipse derived from the d_{xy} orbitals is elongated along the [001] (or $\Gamma - \bar{Z}$) direction. The Rashba effect splits and mixes these bands and creates the more complicated four-sheet Fermi surface in Fig. 7.

Switching on the magnetic field results in an area change of the various Fermi surface sheets as well as a displacement perpendicular to the field direction whereby pairs of bands are shifted in opposite direction, namely bands 1 and 2 and bands 3 and 4. This displacement is considerably more pronounced for the magnetic field in [001] direction and barely visible for magnetic field in [1$\bar{1}$0]-direction. Qualitatively, this behavior can be derived from the simplified single-band model [29]:

$$H = \frac{p^2}{2m} + \alpha\ \boldsymbol{\tau} \cdot (\boldsymbol{p} \times \boldsymbol{e}_z) - \omega_s \boldsymbol{\tau} \cdot \boldsymbol{B}. \tag{1}$$

Here α is the strength of the Rashba coupling, $\omega_s = \mu_B B$ and $\boldsymbol{\tau}$ the vector of Pauli matrices. The magnetic field $\boldsymbol{B} = B\boldsymbol{e}_B$ is in the (x, y) plane and it is assumed that $p_F^2/2m \gg \alpha p_F, \omega_s$, where p_F is the Fermi momentum. The eigenvalues are

$$E_{\boldsymbol{p}}^{(\pm)} = \frac{p^2}{2m} \pm |\,\alpha \boldsymbol{p} + \omega_s \boldsymbol{e}_\perp|$$
$$\approx \begin{cases} \frac{p^2}{2m} \pm \omega_s \pm\ \alpha \boldsymbol{p} \cdot \boldsymbol{e}_\perp, & \alpha p_F \ll \omega_s \\ \frac{p^2}{2m} \pm \alpha p \pm \frac{\omega_s}{p} \boldsymbol{p} \cdot \boldsymbol{e}_\perp, & \omega_s \ll \alpha p_F \end{cases},$$

with $\boldsymbol{e}_\perp = \boldsymbol{e}_B \times \boldsymbol{e}_z$. The Fermi momenta for the two sheets can be parameterized by the angle $\varphi \in [0, 2\pi]$:

$$\boldsymbol{p}_F(\varphi) = \begin{cases} \pm m\alpha\ \boldsymbol{e}_\perp + \left(p_F \pm \frac{m\omega_s}{p_F}\right)\boldsymbol{e}_p, & \alpha p_F \ll \omega_s \\ \pm \frac{m\omega_s}{p_F}\ \boldsymbol{e}_\perp + (p_F \pm m\alpha)\boldsymbol{e}_p, & \omega_s \ll \alpha p_F \end{cases},$$

where $p_F = \sqrt{2mE_F}$ and $\boldsymbol{e}_p = (\cos(\varphi), \sin(\varphi))$. In both limiting cases, these are two circular sheets with slightly different radii, displaced in the direction perpendicular to the magnetic field. More precisely, when looking along $\boldsymbol{B}$, for $\alpha > 0$ the larger (smaller) circle is displaced to the right (left). For $\alpha < 0$, on the other hand, the larger (smaller) circle is displaced to the left (right). Figure 7 shows that for $\boldsymbol{B} \parallel [001]$ the bands 1 and 2 as well as the bands 3 and 4 form two such pairs

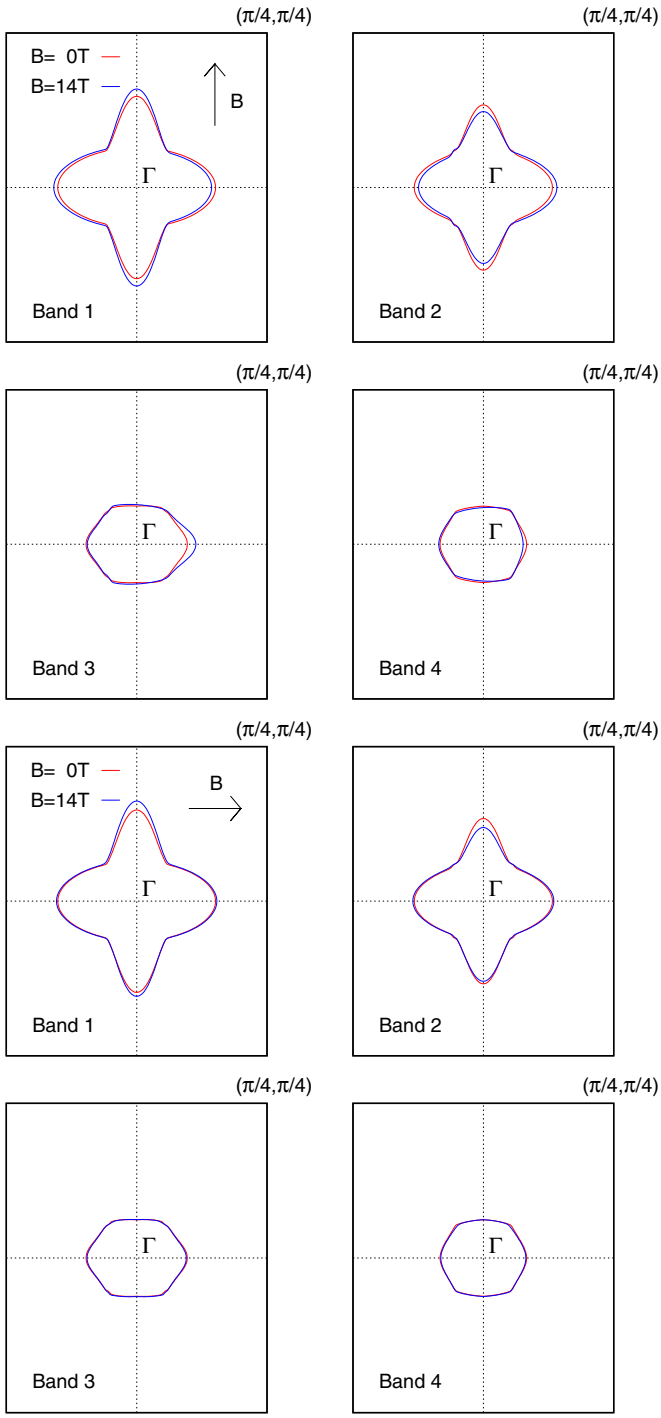

FIG. 7. The four Fermi sheets for $n_e = 0.05$/unit cell in zero magnetic field and a magnetic field of 14 T. The field direction is [001] for the four topmost panels and $[1\bar{1}0]$ for the four bottom panels (see arrows).

of Fermi surface sheets, which are displaced in opposite directions. Thereby, the direction of displacement indicates that the sheets 1 and 2 appear to have an effective $\alpha < 0$ whereas the two inner sheets 3 and 4 have $\alpha > 0$. As already mentioned, the displacement is much smaller for $\boldsymbol{B} \parallel [1\bar{1}0]$ than for $\boldsymbol{B} \parallel$ [001], which again shows the pronounced anisotropy of the Rashba effect in the more realistic LCAO Hamiltonian.

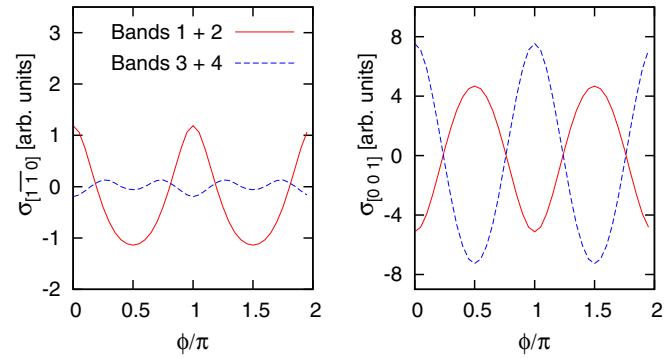

FIG. 8. Variation of $\sigma_{[1\bar{1}0]}$ (left) and $\sigma_{[001]}$ (right) with the angle ϕ between $\mathbf{B}$ and the [001] direction. Thereby, $B = 14$ T. A ϕ-independent constant has been subtracted to make the variations visible; for the labeling of the Fermi surface sheets see Fig. 7.

Using the energy bands $E_{\nu,\mathbf{k}}$, we calculated the 2×2 conductivity tensor using the semiclassical expression

$$\sigma_{\alpha\beta} = e^2 \sum_{\nu} \tau_\nu \, I^{(\nu)}_{\alpha,\beta},$$

$$I^{(\nu)}_{\alpha,\beta} = \frac{1}{4\pi^2} \int d\boldsymbol{k} \, \delta(E_{\nu,\mathbf{k}} - E_F) \, v_{\nu,\alpha} v_{\nu,\beta}$$

$$= \frac{1}{4\pi^2} \int_0^{2\pi} d\varphi \, k_{F,\nu}(\varphi) \, \frac{v_{\nu,\alpha}(\varphi) v_{\nu,\beta}(\varphi)}{\nabla_{\boldsymbol{k}} E_\nu(\varphi) \cdot \mathbf{e}_{\mathbf{k}}}. \qquad (2)$$

Here $\alpha, \beta \in \{x, y\}$, $\mathbf{k}_{F,\nu}(\varphi)$ is the Fermi momentum of the ν^{th} sheet along the direction $\mathbf{e}_{\mathbf{k}} = (\cos(\varphi), \sin(\varphi))$ and $\mathbf{v}_\nu(\varphi)$ is the velocity $\hbar^{-1} \nabla_{\boldsymbol{k}} E_{\nu\boldsymbol{k}}$ evaluated at $\mathbf{k}_{F,\nu}(\varphi)$. Moreover, τ_ν denotes the lifetime of the electrons in band ν which we assume independent of φ for simplicity.

Figure 8 then shows the variation of the "band resolved" conductivities with the angle ϕ between magnetic field and [001] axis.

More precisely, the figure shows the contributions of different bands ν in Eq. (2) to the two diagonal elements $\sigma_{[1\bar{1}0]}$ and $\sigma_{[001]}$ of σ. Thereby, these contributions are actually summed over pairs of bands as suggested by Fig. 7, which shows that the two sheets belonging to one pair have similar Fermi surface geometry and shift in opposite direction in a magnetic field. The variation of the conductivity with field direction has the form

$$\sigma \approx A_0 + A_2 \cos(2\Theta) + A_4 \cos(4\Theta), \qquad (3)$$

where Θ again is the angle between magnetic field and current direction. For bands 1 and 2, the constant A_2 is negative and substantially larger than A_4 so that the conductivity is minimal for $\boldsymbol{j} \parallel \boldsymbol{B}$. This behavior can be reproduced qualitatively already in the framework of the generic model Eq. (1). In the limit $\alpha p_F \ll E_F, \omega_s$ evaluation of Eq. (2) yields

$$\sigma = e^2 \tau \, \pi^{-1} [E_F - m\alpha^2 \, \sin^2(\Theta)]. \qquad (4)$$

Numerical evaluation shows that this result is quite general, i.e., σ has the form Eq. (3) with $A_2 < 0$ and $A_4 = 0$ for any α or ω_s. Figure 9 shows the numerical values of A_2/A_0 versus ω_s. Nonvanishing magnetoresistance occurs only above a threshold value $\omega_s^{(\min)}$, which depends on α. This was found previously by Raimondi *et al.* [29] although these authors did not consider the detailed variation with field direction.

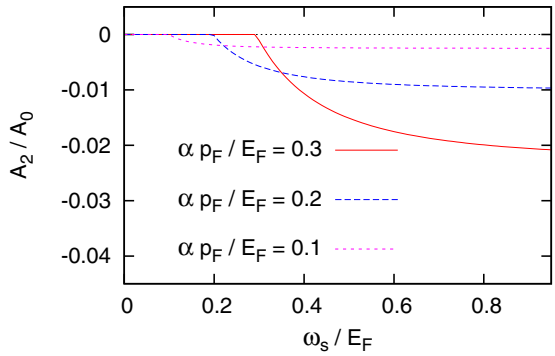

FIG. 9. Ratio of Fourier coefficients A_2/A_0 in Eq. (3) calculated numerically for the simplified model Eq. (1).

The behavior of the contribution from bands 3 and 4 differs strongly from the prediction of the simple model. First, the variation of $\sigma_{[1\bar{1}0]}$ has a substantial admixture of the higher angular harmonic $\cos(4\Theta)$. Second, while the variation of $\sigma_{[001]}$ does have a predominant $\cos(2\Theta)$ behavior, one now has $A_2 > 0$. The deviating behavior for this pair of bands is hardly surprising in that Fig. 7 shows that the displacement of the Fermi surface is practically zero for $\boldsymbol{B} \parallel [1\bar{1}0]$ but quite strong for $\boldsymbol{B} \parallel [001]$, which suggests that for these two bands the effective Rashba parameter α depends on the direction of the magnetic field. Figure 9 also shows that nonvanishing magnetoresistance occurs only above a certain minimum magnetic field. Our LCAO results differ from this in that the amplitude of the oscillations vanishes as B^2 for small B.

Despite an extensive search we were unable to find a set of LCAO parameters such that the sheet resistivities [obtained by inversion of the 2×2 conductivity matrix Eq. (2)] obtained with a single, band-independent relaxation time τ match the experimental R_s versus ϕ curves in Fig. 4. Agreement with experiment could be achieved, however, by choosing a band-dependent relaxation time, more precisely the relaxation time $\tau_{1,2}$ for the bands 1 and 2 had to be chosen larger by roughly a factor 4 as compared to $\tau_{3,4}$ for bands 3 and 4. The relaxation times obtained by fitting the experimental data are shown in Fig. 10. They have the expected order of magnitude and their monotonic and smooth variation with magnetic field is a few percent. Using the Fermi surface averages of the Fermi velocity of $\approx 5 \times 10^4 \frac{m}{s}$ the mean free paths are $l_{1,2} \approx 9$ nm and $l_{3,4} \approx 2.5$ nm.

The resulting ϕ-dependence of the sheet resistance is compared to the experimental data in Fig. 11. While the agreement for current along [001] is good, there is some discrepancy for current along $[1\bar{1}0]$ in that the experimental curves have wide minima and sharp maxima, whereas this is opposite for the calculated curves.

This may indicate the limitations of the quasiclassical Boltzmann approach as already discussed in Ref. [27] where a full solution of the Boltzmann equation was necessary to reproduce the experimental data. For completeness, we note that a band-dependent relaxation time has been observed experimentally in materials such as MgB_2 [30] and some iron-pnictide superconductors [31,32].

Summarizing this section, we may say that while a detailed fit of the experimental data in the framework of the relaxation time approximation to semiclassical Boltzmann theory is not entirely successful, the overall behavior observed in experiment—a variation of the conductivity with magnetic field direction predominantly according to $\sigma = A_0 + A_2 \cos(2\Theta)$, i.e., a noncrystalline anisotropy, is quite generic and can be reproduced qualitatively already in the simplest model Eq. (1). Interestingly, the considerably more complicated and anisotropic band structure does not change this significantly. Also the experimental order of

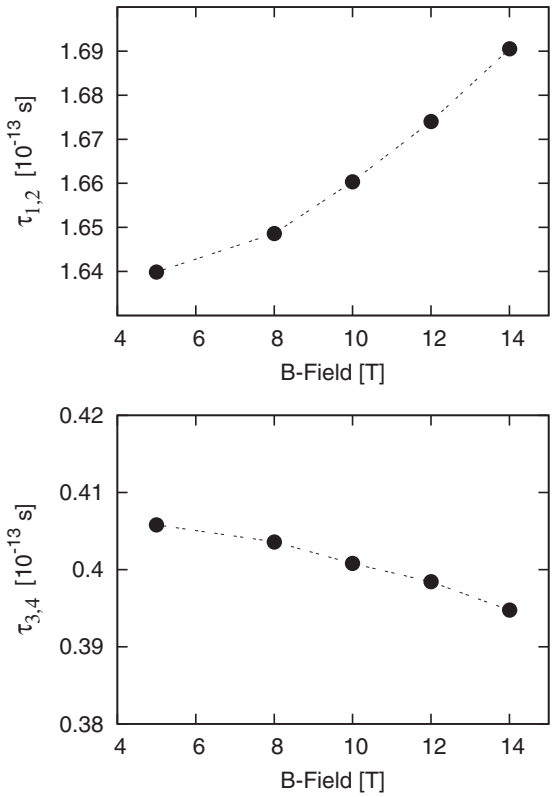

FIG. 10. Variation of the lifetimes $\tau_{1,2}$ and $\tau_{3,4}$ with magnetic field.

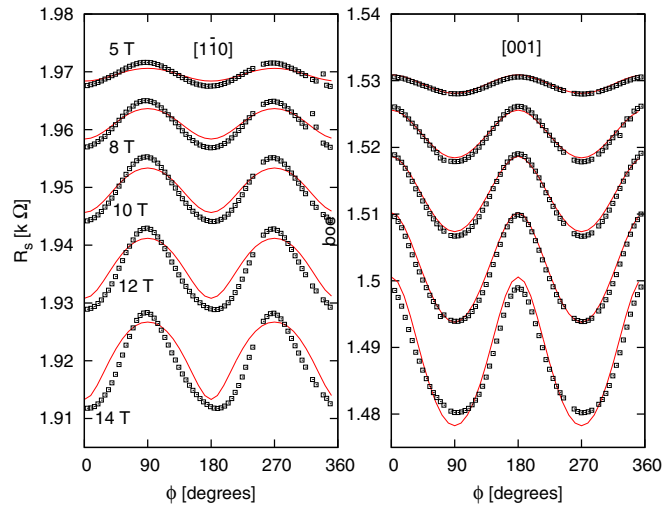

FIG. 11. Calculated sheet resistance (lines) versus angle ϕ between magnetic field and [001] direction compared to the experimental data (squares), cf. Fig. 4.

magnitude of A_2/A_0—a few percent—is reproduced by the calculation. In fact, no reasonable choice of parameters of the LCAO model produces an A_2/A_0 that is larger than a few percent. On the other hand, the results show that the Rashba effect in the (110) surface is strongly anisotropic so that some deviations from this simple behavior are not surprising. The calculation moreover shows that at least within the framework of the relaxation time approximation, the lifetime for electrons in the two inner Fermi surface sheets must be chosen shorter.

IV. SUMMARY

Anisotropic electronic transport of the 2DES in (110) AO/STO was characterized by temperature and magnetic-field dependent four-point resistance measurements along different crystallographic directions. Anisotropic behavior of R_s is evident over the complete measured T-range ($2\ \mathrm{K} \leqslant T \leqslant 300\ \mathrm{K}$) with lowest sheet resistance and largest electron mobility along the [001] direction. The anisotropy of μ is mainly responsible for the anisotropic behavior of the normal magnetotransport MR for $30\ \mathrm{K} > T > 5\ \mathrm{K}$, where LS dominates magnetotransport. At 2 K and $B < 2$ T, MR is dominated by WAL. The spin-orbit field deduced from WAL is well comparable to that found in (001) AO/STO and LAO/STO and seems to depend not on specific crystallographic direction.

Tight-binding calculations were carried out to model the electronic subbandstructure, confirming the anisotropy of μ. Despite the high anisotropy of the Fermi surfaces, the AMR shows a Rashba-induced noncrystalline behavior with resistance maxima for in-plane magnetic field parallel to current direction. Semiclassical Boltzmann theory was used to calculate conductivity and AMR, confirming the rather unexpected experimental result of a noncrystalline AMR, despite strong anisotropic Fermi surface sheets which, however, lead to a strong sensitivity of the AMR behavior of (110) AO/STO on E_F as already observed for (001) LAO/STO. On the other side, electronic subband-engineering by, e.g., epitaxial strain, may also provide possibilities to tune AMR behavior, which might be interesting with respect to spintronics.

Interestingly, our experimental data deviate strikingly from those of Harsan Ma *et al.* obtained on LAO/STO(110) heterostructures [8]. These authors find a crystalline AMR, that means the resistivities along both $[1\bar{1}0]$ and [001] directions show a maximum when the magnetic field is perpendicular to the [001] direction, and moreover the amplitude of the variation is much larger, up to 100%. We believe that this is an indication that these authors actually observed a different effect as compared to our experiments. In fact, Harsan Ma *et al.* interpreted their results as being due to oxygen vacancies and a redistribution of conduction electrons between the t_{2g} orbitals with increasing magnetic field. The steady increase of the AMR amplitude with decreasing $p(O_2)$ (oxygen partial pressure during film deposition) and the resulting giant AMR effect is discussed in terms of strong oxygen vacancy induced orbital polarization, which likewise is responsible for the crystalline nature of the AMR. In contrast to this, the qualitative agreement between our experiments, the LCAO calculations, and also the simple "toy model" Eq. (1) indicates that the AMR in our experiment is largely due to the Rashba effect, whereas impurities play only a minor role. The much smaller AMR amplitudes in our experiment and the noncrystalline AMR nature can be reproduced quantitatively by LCAO calculations, assuming reasonable electron relaxation times and this result is robust under a considerable variation of the parameters in the LCAO model. In fact, no choice of the electronic relaxation times or other parameters could produce an AMR amplitude of more than a few percent or a crystalline AMR. The reason why oxygen vacancies seem to play such a different role in (110) LAO/STO and AO/STO heterostructures clearly is an interesting question and needs further clarification.

ACKNOWLEDGMENTS

Part of this paper was supported by the Deutsche Forschungsgemeinschaft (DFG) Grant No. FU 457/2-1. We are grateful to R. Thelen and the Karlsruhe Nano Micro Facility (KNMF) for technical support. We also acknowledge D. Gerthsen and M. Meffert from the laboratory for electron microscopy (LEM) for transmission electron microscopy analysis of our samples.

APPENDIX: LCAO CALCULATION

We describe bulk $SrTiO_3$ as a simple cubic lattice of Ti atoms with lattice constant unity at the positions $\boldsymbol{R}_i$ and retain only the three t_{2g} orbitals of each Ti atom. The Hamiltonian is most easily formulated in a coordinate system with axes parallel to Ti-Ti bonds, which we call the bulk coordinate system. In the following, $\alpha, \beta, \gamma \in \{x, y, z\}$ always refer to the bulk coordinate system, are assumed to be pairwise unequal, and $\boldsymbol{e}_\alpha$ denotes the lattice vector in α-direction. Following Wang *et al.* [11] we use a tight-binding parametrization of the Hamiltonian with hopping integrals

$$\begin{aligned} \langle d_{\alpha\beta}(\boldsymbol{R}_i \pm \boldsymbol{e}_\alpha)|H|d_{\alpha\beta}(\boldsymbol{R}_i)\rangle &= t, \\ \langle d_{\alpha\beta}(\boldsymbol{R}_i \pm \boldsymbol{e}_\gamma)|H|d_{\alpha\beta}(\boldsymbol{R}_i)\rangle &= t_1, \\ \langle d_{\alpha\beta}(\boldsymbol{R}_i \pm \boldsymbol{e}_\alpha \pm \boldsymbol{e}_\beta)|H|d_{\alpha\beta}(\boldsymbol{R}_i)\rangle &= t_2. \end{aligned} \tag{A1}$$

Following Zhong *et al.* [28], we model the interface as a hemispace of bulk $SrTiO_3$ with surface perpendicular to the unit vector $\boldsymbol{e}_n = \frac{1}{\sqrt{2}}(1, 1, 0)$ and the origin of the coordinate system coinciding with some atom on the surface. Accordingly, only atoms with $\boldsymbol{R}_i \cdot \boldsymbol{e}_n \geqslant 0$ are retained. The electrons are confined to the interface by a wedge-shaped electrostatic potential which gives an extra energy $\epsilon_i = eE\boldsymbol{R}_i \cdot \boldsymbol{e}_n$ with $E > 0$ for all three t_{2g} orbitals on the Ti atom at $\boldsymbol{R}_i$.

The unit cell of the resulting (1,1,0) surface is a rectangle with edges $\sqrt{2} \parallel [1\bar{1}0]$ and $1 \parallel [001]$. The Brillouin zone has the extension $\sqrt{2}\pi$ in $[1\bar{1}0]$-direction and 2π in [001]-direction and we define $\bar{M} = (\pi/\sqrt{2}, 0)$ and $\bar{Z} = (0, \pi)$.

Using the model described so far, Wang *et al.* obtained an excellent fit to their ARPES band structure at the $SrTiO_3$ (110) surface by using the values $t = -277$ meV, $t_1 = -31$ meV, $t_2 = -76$ meV, and $eE = 10\ \mathrm{meV}/\sqrt{2}$. Using these values, the conductivity calculated within the Boltzmann equation formalism (as described in the main text) shows a rather strong anisotropy, $\sigma_{[001]}/\sigma_{[1\bar{1}0]} \approx 3.5$, much larger than the experimental value $\sigma_{[001]}/\sigma_{[1\bar{1}0]} \approx 1.3$. The reason is that for the low-electron densities of ≈ 0.05/unit cell in our experiment,

the d_{xy}-derived band, which has small effective mass along the [1$\bar{1}$0] direction (see Fig. 5), is almost empty. This can be changed, however, by reducing $t \to -269.5$ meV for all bonds in [001] direction. This reduction by 2.5% might be the consequence of a slight distortion of the lattice in the neighborhood of the interface. The same reduction of the anisotropy could also be obtained by lowering the energy of the d_{xy}-orbital by ≈10 meV. Both modifications shift the minimum of the d_{xy}-derived band to lower energy and thus increase its filling.

To discuss the magnetoconductance, we extended the model of Wang *et al.* by including the Rashba effect—that means the combined effect of spin-orbit coupling in the Ti 3d shell and the confining electric field—as well as an external magnetic field. First, the nonvanishing matrix elements of the of orbital angular momentum operator $\boldsymbol{L}$ within the subspace of the t_{2g} orbitals are

$$\langle d_{xz}|L_x|d_{xy}\rangle = i\hbar,$$

plus two more equations obtained by cyclic permutations of (x, y, z). Choosing the basis on each Ti atom as $(d_{xy,\uparrow}, d_{xy,\downarrow}, d_{xz,\uparrow}, d_{xz,\downarrow}, d_{yz,\uparrow}, d_{yz,\downarrow})$ one thus finds

$$L_x = \hbar \begin{pmatrix} 0 & -i & 0 \\ i & 0 & 0 \\ 0 & 0 & 0 \end{pmatrix} \otimes \tau_0,$$

$$L_y = \hbar \begin{pmatrix} 0 & 0 & i \\ 0 & 0 & 0 \\ -i & 0 & 0 \end{pmatrix} \otimes \tau_0,$$

$$L_z = \hbar \begin{pmatrix} 0 & 0 & 0 \\ 0 & 0 & -i \\ 0 & i & 0 \end{pmatrix} \otimes \tau_0,$$

where τ_0 is the unit matrix in spin space. The Hamiltonian for the spin-orbit coupling then is [28]

$$\begin{aligned} H_{\mathrm{SO}} &= \lambda_{\mathrm{SO}}\, \boldsymbol{L}\cdot\boldsymbol{S} \\ &= \frac{\lambda_{\mathrm{SO}}\, i\hbar^2}{2}((|xz\rangle\langle xy| - |xy\rangle\langle xz|)\tau_x + \mathrm{c.p.}) \\ &= \frac{\lambda_{\mathrm{SO}}\,\hbar^2}{2} \begin{pmatrix} 0 & -i\tau_x & i\tau_y \\ i\tau_x & 0 & -i\tau_z \\ -i\tau_y & i\tau_z & 0 \end{pmatrix}. \end{aligned}$$

Here c.p. denotes two more terms obtained by cyclic permutation of x, y, z and $\boldsymbol{\tau}$ is the vector of Pauli matrices. We use $\lambda_{\mathrm{SO}}\hbar^2 = 20$ meV. The coupling to an external magnetic field $\boldsymbol{B}$ is

$$H_B = \mu_B(\mathbf{L} + g\,\mathbf{S})\cdot\boldsymbol{B},$$

with the Bohr magneton μ_B and we use $g = 5$ [33].

In addition to the matrix elements Eq. (A1), the confining electric field gives rise to small but nonvanishing hopping elements, which would vanish due to symmetry in the bulk. The respective term in the Hamiltonian is $H_E = |e|\mathbf{E}_\perp\cdot\mathbf{r}$, where $\mathbf{E}_\perp$ is the component of the electric field perpendicular to the bond. As shown by Zhong *et al.* [28] the respective matrix elements can be written as (α, β, and γ refer to the bulk system and are pairwise unequal)

$$\langle d_{\alpha\beta}(\boldsymbol{R}_i \pm \boldsymbol{e}_\gamma)|H_E|d_{\beta\gamma}(\boldsymbol{R}_i)\rangle = \pm|e|\; E_\alpha\; V_E,$$
$$\langle d_{\beta\gamma}(\boldsymbol{R}_i \pm \boldsymbol{e}_\gamma)|H_E|d_{\alpha\beta}(\boldsymbol{R}_i)\rangle = \mp|e|\; E_\alpha\; V_E,$$

and we used the value $|e|\; E\; V_E = 5$ meV. The sign of V_E is positive if one really considers only two d orbitals at the given distance. This might change if one really considers hopping via the oxygen-ion between the two Ti ions in the true crystal structure of $SrTiO_3$. We have verified, however,that inverting the sign of V_E does not change the angular dependence of the magnetoresistance in Fig. 11, although it does in fact change the direction of the shift of the Fermi surface sheets in Fig. 3, which means the sign of the effective α. In fact, as can be seen from Eq. (4), the sign of α does not influence the angular variation of the conductivity.

We neglect any matrix elements of the electric field between orbitals centered on atoms more distant than nearest neighbors. The interplay between these additional hopping matrix elements and the spin-orbit coupling gives rise to the Rashba splitting of the bands. Adding the respective terms to the tight-binding Hamiltonian, we obtain the band structure and its variation with a magnetic field. We have verified that slight variations of λ_{SO}, $|e|EV_E$, or g do not lead to qualitative changes of the results reported in the main text.

[1] N. Reyren, S. Thiel, A. D. Caviglia, L. F. Hammerl, C. Richter, C. W. Schneider, T. Kopp, A. S. Ruetschi, D. Jaccard, M. Gabay, D. A. Muller, J. M. Triscone, and J. Mannhart, Science **317**, 1196 (2007).

[2] A. D. Caviglia, M. Gabay, S. Gariglio, N. Reyren, C. Cancellieri, and J. M. Triscone, Phys. Rev. Lett. **104**, 126803 (2010).

[3] J. Biscaras, N. Bergeal, S. Hurand, C. Feuillet-Palma, A. Rastogi, R. C. Budhani, M. Grilli, S. Caprara, and J. Lesueur, Nature Mater. **12**, 542 (2013).

[4] A. Brinkman, M. Huijben, M. Van Zalk, J. Huijben, U. Zeitler, J. C. Maan, W. G. Van der Wiel, G. Rijnders, D. H. A. Blank, and H. Hilgenkamp, Nat. Mater. **6**, 493 (2007).

[5] A. Joshua, S. Pecker, J. Ruhman, E. Altman, and S. Ilani, Nat. Commun. **3**, 1129 (2012).

[6] A. Fête, S. Gariglio, A. D. Caviglia, J. M. Triscone, and M. Gabay, Phys. Rev. B **86**, 201105(R) (2012).

[7] A. Joshua, J. Ruhman, S. Pecker, E. Altman, and S. Ilani, Proc. Natl. Acad. Sci. USA **110**, 9633 (2013).

[8] H. J. Harsan Ma, J. Zhou, M. Yang, Y. Liu, S. W. Zeng, W. X. Zhou, L. C. Zhang, T. Venkatesan, Y. P. Feng, and Ariando, Phys. Rev. B **95**, 155314 (2017).

[9] M. Trushin, K. Výborný, P. Moraczewski, A. A. Kovalev, J. Schliemann, and T. Jungwirth, Phys. Rev. B **80**, 134405 (2009).

[10] Y. Z. Chen, N. Pryds, J. E. Kleibeuker, G. Koster, J. Sun, E. Stamate, B. Shen, G. Rijnders, and S. Linderoth, Nano Lett. **11**, 3774 (2011).
[11] Z. Wang, Z. Zhong, X. Hao, S. Gerhold, B. Stöger, M. Schmid, J. Sanchez-Barriga, A. Varykhalov, C. Franchini, K. Held, and U. Diebold, Proc. Natl. Acad. Sci. USA **111**, 3933 (2014).
[12] D. Fuchs, R. Schäfer, A. Sleem, R. Schneider, R. Thelen, and H. v. Löhneysen, Appl. Phys. Lett. **105**, 092602 (2014).
[13] D. Fuchs, K. Wolff, R. Schäfer, R. Thelen, M. Le Tacon, and R. Schneider, AIP Adv. **7**, 056410 (2017).
[14] M. Huijben, G. Rijnders, D. H. A. Blank, S. Bals, S. V. Aert, J. Verbeeck, G. V. Tendeloo, A. Brinkman, and H. Hilgenkamp, Nat. Mater. **5**, 556 (2006).
[15] Y. Li, Y. Lei, B. G. Shen, and J. R. Sun, Sci. Rep. **5**, 14576 (2015).
[16] K. Gopinadhan, A. Annadi, Y. Kim, A. Srivastava, B. Kumar, J. Chen, J. M. D. Coey, Ariando, and T. Venkatesan, Adv. Electron. Mater. **1**, 1500114 (2015).
[17] S.-C. Shen, Y.-P. Hong, C.-J. Li, H.-X. Xue, X.-X. Wang, and J.-C. Nie, Chin. Phys. B **25**, 076802 (2016).
[18] D. van der Marel, J. L. M. van Mechelen, and I. I. Mazin, Phys. Rev. B **84**, 205111 (2011).
[19] D. Fuchs, A. Sleem, R. Schäfer, A. G. Zaitsev, M. Meffert, D. Gerthsen, R. Schneider, and H. v. Löhneysen, Phys. Rev. B **92**, 155313 (2015).
[20] K. Wolff, R. Schäfer, M. Meffert, D. Gerthsen, R. Schneider, and D. Fuchs, Phys. Rev. B **95**, 245132 (2017).
[21] Z. Chen, H. Yuan, Y. Xie, D. Lu, H. Inoue, Y. Hikita, Ch. Bell, and H. Y. Hwang, Nano Lett. **16**, 6130 (2011).
[22] A. Othomo and H. Y. Hwang, Nature **427**, 423 (2004).
[23] G. Herranz, F. Sánchez, N. Dix, M. Scigaj, and J. Fontcuberta, Sci. Rep. **2**, 758 (2012).
[24] P. A. Lee and T. V. Ramakrishnan, Rev. Mod. Phys. **57**, 287 (1985).
[25] S. Maekawa and H. Fukuyama, J. Phys. Soc. Jpn. **50**, 2516 (1981).
[26] A. P. Pippard, *Magnetoresistance in Metals* (Cambridge University Press, Cambridge, 1998).
[27] M. Diez, A. M. R. V. L. Monteiro, G. Mattoni, E. Cobanera, T. Hyart, E. Mulazimoglu, N. Bovenzi, C. W. J. Beenakker, and A. D. Caviglia, Phys. Rev. Lett. **115**, 016803 (2015).
[28] Z. Zhong, A. Toth, and K. Held, Phys. Rev. B **87**, 161102(R) (2013).
[29] R. Raimondi, M. Leadbeater, P. Schwab, E. Caroti, and C. Castellani, Phys. Rev. B **64**, 235110 (2001).
[30] E. A. Yelland, J. R. Cooper, A. Carrington, N. E. Hussey, P. J. Meeson, S. Lee, A. Yamamoto, and S. Tajima, Phys. Rev. Lett. **88**, 217002 (2002).
[31] T. Terashima, N. Kurita, M. Tomita, K. Kihou, C.-H. Lee, Y. Tomioka, T. Ito, A. Iyo, H. Eisaki, T. Liang, M. Nakajima, S. Ishida, S.-I. Uchida, H. Harima, and S. Uji, Phys. Rev. Lett. **107**, 176402 (2011).
[32] T. Terashima, N. Kurita, M. Kimata, M. Tomita, S. Tsuchiya, M. Imai, A. Sato, K. Kihou, C.-H. Lee, H. Kito, H. Eisaki, A. Iyo, T. Saito, H. Fukazawa, Y. Kohori, H. Harima, and S. Uji, Phys. Rev. B **87**, 224512 (2013).
[33] A. Fête, S. Gariglio, C. Berthod, D. Li, D. Stornaiuolo, M. Gabay, and J.-M. Triscone, New J. Phys. **16**, 112002 (2014).